Contents lists available at ScienceDirect

Applied Catalysis B: Environmental

journal homepage: www.elsevier.com/locate/apcatb

Sequential active-site switches in integrated Cu/Fe-TiO$_2$ for efficient electroreduction from nitrate into ammonia

Xiaohui Yang [a,b,1], Rong Wang [c,1], Sha Wang [a,b], Cheng Song [a,b], Shun Lu [a,b], Ling Fang [a,b], Fengjun Yin [a,b,*], Hong Liu [a,b,*]

[a] Chongqing Institute of Green and Intelligent Technology, Chinese Academy of Sciences, Chongqing 400714, PR China
[b] Key Laboratory of Reservoir Aquatic Environment, Chinese Academy of Sciences, Chongqing 400714, PR China
[c] School of Metallurgy and Materials Engineering, Chongqing University of Science & Technology, Chongqing 401331, PR China

ARTICLE INFO

ABSTRACT

Understanding the reaction mechanism is critical for efficient electroreduction from NO$_3^-$ into NH$_3$. Here, a novel sequential active-site-switching (SASS) mechanism is proposed according to the thermodynamic nature of bonding, which involves two key site switches on different active species in an integrated electrocatalyst. We implement this concept by employing Cu/Fe hetero-phase-interface nanoparticles anchored in TiO$_2$ substrate (Cu/Fe-TiO$_2$) as a model platform. Theoretical calculations coupled with in situ infrared spectra confirm the SASS mechanism: the *NO$_3$, preferentially adsorbed on the in-plane Fe phase, switches towards the Cu/Fe hetero-phase interface to reduce into *NH$_3$, and a further switch related to the *NH$_3$ occurs towards the in-plane Cu phase, notably facilitating the NO$_3^-$-into-NH$_3$ conversion. Such a SASS pathway endows Cu/Fe-TiO$_2$ with excellent intrinsic activity, 4.68- and 2.82-fold higher than that of Cu-TiO$_2$ and Fe-TiO$_2$, respectively.

1. Introduction

Nitrogen cycling is a basic substance cycling in nature. Nitrate (NO$_3^-$) poses as a notorious pollutant after its release into waters, which readily triggers aqueous eutrophication and even serious human health issues [1,2]. Any effective removal process of NO$_3^-$ at the discharge sites has been recognized as one of the pressing and urgent challenges by the National Academy of Engineering in the current century [3–6]. Various technologies, such as biological denitrification, reverse osmosis, ion exchange, and electrodialysis, have been practiced in wastewater treatment plants [7]. However, challenges still remain due to the technical defects of harsh operating conditions, low efficiency, high cost, and production of secondary waste, etc [8,9]. From an energy-economy-environment perspective, the conversion of NO$_3^-$ into value-added ammonia (NH$_3$), a promising carrier of hydrogen energy, is of emerging interest to realize the utilization of "waste-to-wealth" while offer an appealing and supplementary alternative to the capital- and energy-intensive Haber-Bosch process [10–15].

The NO$_3^-$ reduction reaction (NO$_3^-$RR) into NH$_3$ via electrochemical means has aroused tremendous attention due to its environmental benignity, moderate operating conditions, non-reliance on additional reductants, and compatibility with clean electrical energy from renewable energy sources, such as solar and wind power [16–19]. Given the approximate energy level between the highest occupied D-orbital of copper (Cu) and the lowest unoccupied π * -orbital of NO$_3^-$, Cu has been considered as one of the most active electrocatalysts for the NO$_3^-$RR, with a rapid transformation kinetics from NO$_3^-$ into nitrite (NO$_2^-$) [20, 21]. Unfortunately, NO$_2^-$ is more toxic than the former by resulting in methemoglobinemia due to the accumulation in body tissues [22]. Moreover, pure Cu-based electrodes are prone to spontaneous oxidative dissolution with prolonged reduction time, leading to the decreased electrocatalytic activity. To address these issues, binary alloys, such as CuPt, CuPd, CuRu, and CuFe, etc, have been developed and demonstrated an improved NO$_3^-$RR performance in their activity, selectivity, and stability [23–26]. However, the decipherment for the NO$_3^-$RR improvement is vague while a lack of inner cognition.

As the NO$_3^-$RR involves a multistep transfer of 8 electrons and 9 protons, understanding this complicated reaction mechanism on the catalyst surface is critical for the rational design of electrode matrix and the efficient enhancement of NO$_3^-$RR process. To date, it has been

acknowledged that the stable adsorbed hydrogen (H_{ads}) generated from the water reduction potentially facilitates NH_3 production in the hydrogenation mechanism, where Cu performs the $*NO_3$ adsorption and another metal acts as the H_{ads} binding site [6,23]. This mechanism can well explain the improved NO_3^-RR performance on Cu-based binary alloys, especially in relation to the noble metals with the suitable stabilization of H_{ads}; however, it does not explain for that of CuFe alloy because Fe captures and stabilizes H_{ads} inefficiently [27,28]. We noted that the biological conversion of NO_3^--into-NH_3 is a tandem process, implying that this conversion occurs among the different microbial families [29,30]. It appears that there exists a switching phenomenon between the different active sites. But unfortunately, the switching of active sites with the adsorbed intermediates has been ignored but extremely important in understanding the NO_3^-RR mechanism. To the best of our knowledge, no prior work on this novel conceptual topic has been reported.

Herein, as a proof-of-concept exploration, we design and construct a model electrocatalyst of Cu/Fe hetero-phase-interface nanoparticles anchored in TiO_2 substrate (Cu/Fe-TiO_2) by a facile ion-exchange and calcination process. Note that hetero-phase interface, which holds controlled chemical composition and perspicuous electron distribution, is an ideal candidate to elucidate the intrinsic mechanism for electroreduction of NO_3^--into-NH_3 [31]. The as-prepared Cu/Fe-TiO_2 exhibits a high NH_4^+ yield rate of 505.73 µg h^{-1} cm^{-2} (normalized by the roughness factor), which performs 4.68 and 2.82 times more than that of its counterparts of Cu-TiO_2 and Fe-TiO_2, respectively. Moreover, Cu/Fe-TiO_2 has also the excellent selectivity of 90.9 $\pm$ 0.5% and Faradaic efficiency (FE) of 91.2% towards the generated NH_3 as well as an outstanding stability. Notably, density functional theory (DFT) calculations and in situ attenuated total reflection Fourier transform infrared spectroscopy (ATR-SEIRAS) jointly confirm a sequential active-site-switching (SASS) pathway for the efficient conversion of NO_3^--into-NH_3 over Cu/Fe-TiO_2, where the NO_3^- preferentially adsorbs to the in-plane Fe phase, and then intelligently switches towards the Cu/Fe hetero-phase interface to catalyze $*NO_3$ reduction into $*NH_3$, and at last, the adsorbed $*NH_3$ switches towards the in-plane Cu phase to accomplish the desorption of $*NH_3$.

2. Experimental section

2.1. Synthesis of Cu/Fe-TiO₂

The synthesis of Cu/Fe-TiO_2 was conducted by a facile ion-exchange process followed by calcination process. Briefly, 0.2 g of the presynthetic $Na_2Ti_3O_7$ nanorods was added 20 mL of the mixed solution with 10 mmol $FeCl_3 \cdot 6H_2O$ and 10 mmol $CuCl_2 \cdot 2 H_2O$ under energetic magnetic stirring for 30 min. Then the mixture was ultrasonicated for 2 h, and transferred to an orbital shaker for adequate ion-exchange treatment for 24 h. Afterwards, the precipitate was filtered and washed with distilled water until Cl^- was completely removed, and dried at 60 °C overnight. At last, the obtained powder was annealed at 750 °C for 200 min under reductive atmosphere of Ar and H_2 (4:1). In addition, the corresponding contrast materials for the synthetic details were described in the Supporting Information.

2.2. Material characterization

The crystal information was determined by the X-ray diffraction (XRD, X′Pert3 Powder) with Cu Kα (λ = 1.5406 Å) irradiation. The morphology and microstructure were examined by field emission scanning electron microscopy (FESEM, JEOL JSM-7800 F, 5 kV), transmission electron microscopy/high-angle annular dark-feld scanning transmission electron microscopy (TEM/HAADF-STEM, FEI, Talos F200S, 200 kV) coupled with energy dispersive X-ray (EDX) analysis. The surface compositions and chemical states were analyzed by X-ray photoelectron spectroscopy (XPS, Thermo Fisher, ESCALAB250Xi) with

an Al Kα X-ray source (1486.6 eV).

2.3. Electrochemical analysis of NO₃⁻RR

All electrochemical measurements were performed on an electrochemical workstation of CHI 760E using a typical three-electrode system under room temperature. Carbon paper coated with the as-obtained catalysts, Ir-Ru/Ti plate, and saturated calomel electrode (SCE) were employed as the working electrode, the counter electrode, and the reference electrode, respectively. The electrolyte is a mixed solution comprised of 50 ppm $NaNO_3$ and 0.5 M Na_2SO_4. The NO_3^-RR tests were carried out in one-compartment cell accompanied by the continuous magnetic stirring of 500 rpm. For the preparation of working electrode, 20 mg of the as-prepared samples were dispersed in a mixture of 50 µL of Nafion (5 wt%) and 950 µL of ethanol, and sonicated for 20 min to form a homogeneous ink. Then, 200 µL of uniformly dispersed ink was dropped on carbon paper substrate with an area of 2×2 cm^2 (loading: 1 mg cm^{-1}), and dried under ambient condition in air. Before NO_3^-RR tests, high-purity Ar was continuously fed into the electrolyte for 20 min to remove residual air. Cyclic voltammetry (CV) measurements were conducted at least 5 cycles with a scan rate of 10 mV s^{-1} to reach a stable state. Linear sweep voltammetry (LSV) was performed at a scan rate of 100 mV s^{-1} from 0 to -1.8 V vs. SCE. The potentiostatic tests were carried out at different potentials, including -1.0, -1.1, -1.2, -1.3, -1.4, -1.5, -1.6, and -1.7 V vs. SCE. Electrochemical impedance spectra (EIS) measurements were performed on ParSTAT 2273 at a potential of -1.4 V vs. SCE with a frequency from 10^4 to 10^{-2} Hz.

2.4. DFT calculation

All the first-principles spin-polarized calculations were performed using the Vienna ab initio simulation package (VASP) with the Perdew-Burke-Ernzerhof (PBE) exchange-correlation functional [32,33]. The projector augmented-wave (PAW) method implemented in the VASP code was utilized to describe the interaction between the ionic cores and the valence electrons [34,35]. Surface models including rutile TiO_2-supported face-centered cubic Cu (111), body-centered cubic Fe (110) and Cu/Fe heterojunction were constructed with a 15 Å vacuum layer. An energy cutoff of 600 eV and $3 \times 2 \times 1$ k-point with a G centered k mesh were used for structure optimization. The lattice vectors and atomic positions are fully relaxed until the force and energy are converged to 0.02 eV/Å and 10^{-5} eV. During electronic structure calculation, the GGA+U approach was carried to provide an accurate treatment of localized electron states. The dipole correction and the DFT-D3 of the van der Waals dispersion correction were applied for all calculations. For chemical bonding analyses, we utilized the COHP method as calculated by the LOBSTER package, which reconstructs the orbital-resolved electronic structure via projection of the PAW wave functions onto atomic-like basis functions. Here, we performed the VASPKIT to analyze the raw calculated data, which is a post-processing software for VASP code. The visualizations of crystal structures and electron densities was achieved using the VESTA3 program.

3. Results and discussion

### 3.1. Catalyst synthesis and characterization

The construction process of Cu/Fe-TiO_2 with distinct Cu/Fe heterophase interfaces is illustrated in Fig. S1. Briefly, $Na_2Ti_3O_7$ nanorods are prepared by a conventional hydrothermal process (Figs. S2 and S3). Then, the ion-exchange treatment is performed by immersing the asprepared $Na_2Ti_3O_7$ nanorods into a mixed solution with $FeCl_3 \cdot 6 H_2O$ and $CuCl_2 \cdot 2 H_2O$, arousing an automatic substitution of the Na^+ ions in the nanorods with Fe^{3+}/Cu^{2+}. After the calcination under a reductive atmosphere, Cu/Fe-TiO_2 with Cu/Fe hetero-phase interfaces is obtained. Note here that Cu/Fe nanoparticles are in situ grown on the surface of

TiO$_2$ substrate, thus resulting in a strong interaction between the two (Fig. S4), which is beneficial to improve the stability of catalyst against dissolution during NO$_3^-$RR. For comparison, the control samples of Cu-TiO$_2$, Fe-TiO$_2$, and TiO$_2$ substrate are also synthesized following the same procedure with slight modifications (Figs. S5–S9). The synthetic details are described in the experimental section.

The morphology and structure of Cu/Fe-TiO$_2$ were captured by field emission scanning electron microscopy (FE-SEM), transmission electron microscopy (TEM), and high-angle annular dark-field scanning transmission electron microscopy (HAADF-STEM). As shown in Fig. 1a and S10, it can be found that the one-dimensional (1D) nanorods are transformed into 3D porous structure stacked by disordered nanoparticles after the reductive calcination. Fig. 1b shows high-resolution TEM image with a fuzzy interface. The corresponding selected area electron diffraction (SAED) pattern shows two well-defined close rings, which are ascribed to the (110) facet of cubic Fe and the (111) facet of cubic Cu, respectively (Fig. 1c). Clear lattice fringes can be observed, where the interplanar distance of 0.203 nm on the left (the green box) is indexed to the (110) facet of body-centered cubic Fe (Fig. 1d), and the interplanar distance of 0.208 nm on the right (the blue box) is indexed to the (111) facet of face-centered cubic Cu (Fig. 1e). From the HAADF-

STEM image, we can further observe a clear interface, and the elemental maps obtained through energy-dispersive spectroscopy (EDS) strongly confirm the successful construction of Cu/Fe hetero-phase interface (Fig. 1f).

X-ray diffraction (XRD) was carried out to investigate the detailed structural features of Cu/Fe-TiO$_2$. All the different diffraction peaks can be well-indexed to standard cubic Cu (PDF Card No. 85–1326), cubic Fe (PDF Card No. 87–0721), and tetragonal rutile TiO$_2$ (PDF Card No. 89–8303) phases without any peaks for impurities (Fig. 1g). This indicates that the two phases of Cu and Fe are separated, rather than forming a homogeneous alloy, in good agreement with the results of SAED and high-resolution TEM. The surface chemical states of Cu/Fe-TiO$_2$ were probed by X-ray photoelectron spectroscopy (XPS). The XPS spectra of the Ti 2p and O 1 s core-level regions for Cu/Fe-TiO$_2$, Cu-TiO$_2$, and Fe-TiO$_2$ are almost the same (Figs. S11 and S12), indicating that the supported TiO$_2$ is credible as a model substrate in this work. In contrast, Cu 2p peaks in Cu/Fe-TiO$_2$ negatively shift by 0.33 eV compared with that in Cu-TiO$_2$ (Fig. 1h), while Fe 2p peaks in Cu/Fe-TiO$_2$ slightly shift to higher binding energies compared with that in Fe-TiO$_2$ (Fig. 1i). Such corresponding shifts demonstrate that electron transfers from Fe to Cu occur in Cu/Fe hetero-phase interface, which is mainly attributed that
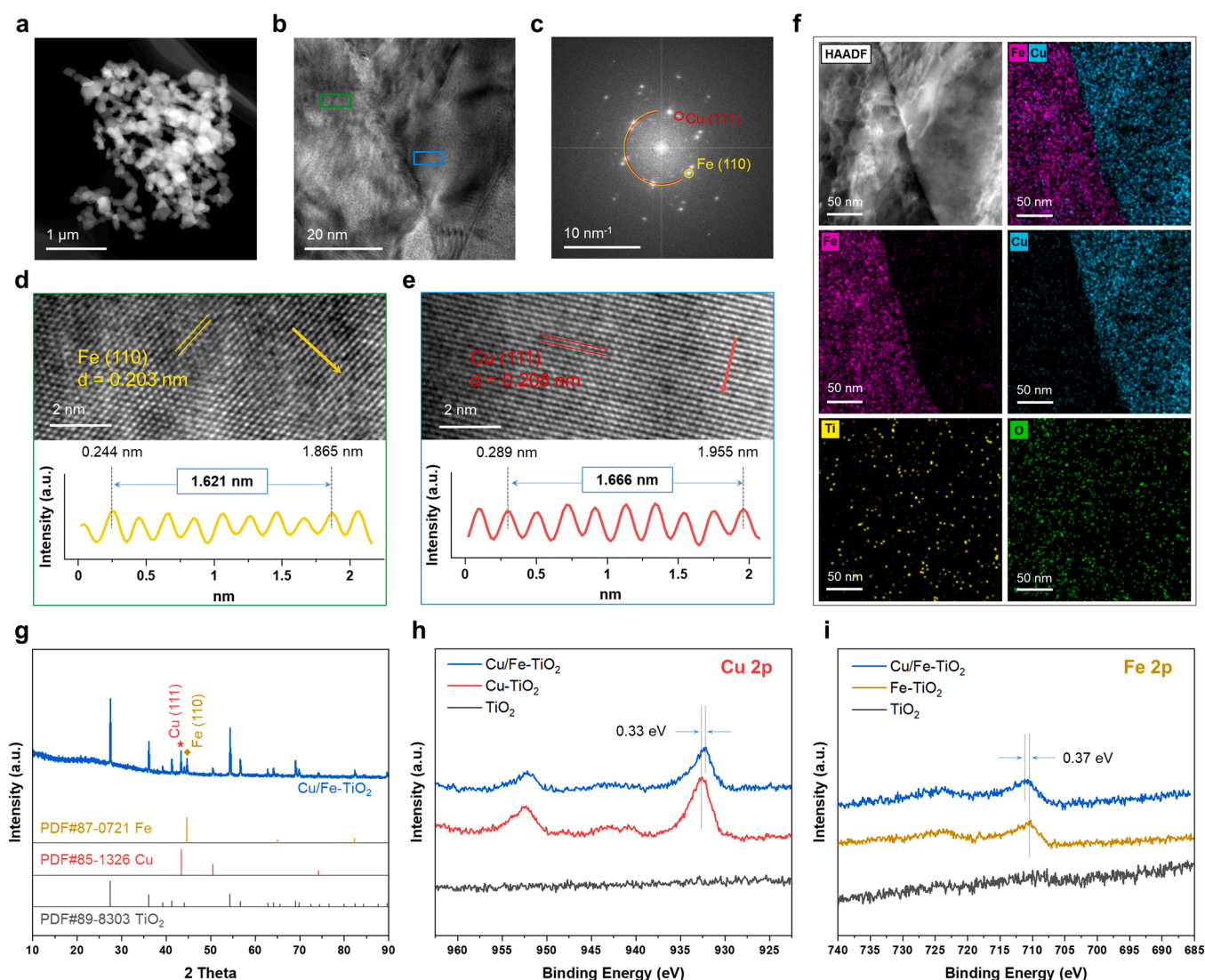
Fig. 1. Structural characterizations of Cu/Fe-TiO$_2$ with a distinct Cu/Fe hetero-phase interface. (a) Low-resolution HAADF-STEM image. (b) High-resolution (HR) TEM image. (c) SAED pattern based on b. (d), (e) Magnified HR-TEM images of the green and blue boxes in b, respectively. Inset in d is intensity profile measured from the corresponding lattice fringe along the Fe (110) direction (yellow arrow). Similarly, inset in e is that along with Cu (111) direction (red arrow). (f) HAADF-STEM-EDS elemental maps. (g) XRD pattern. (h), (i) High-resolution XPS spectra of Cu 2p and Fe 2p, respectively.

Cu (1.90) is more electronegative than Fe (1.83).

3.2. Electrocatalytic NO_3^-RR performance

To determine electrochemical NO_3^- reduction ability of Cu/Fe-TiO$_2$, electrochemical measurements were performed with a typical three-electrode system under room temperature (see the detailed descriptions in the Supporting Information). Linear sweep voltammetry (LSV) was firstly conducted to disclose the different reduction processes with increasing potential. LSV curves in Fig. 2a indicate that the reduction peak (R_1) at around − 0.9 V versus saturated calomel electrode (SCE) can be ascribed to the contribution of NO_3^--into-NO_2^- since this peak disappears as NO_3^--N is removed or replaced in the system. In the presence of NO_2^-, only a single peak is observed, which implies that the other reduction peak (R_n) can be attributed to the reduction of NO_2^- [23]. Considering the difference between the maximum current density recorded in the pure and NO_3^--N or NO_2^--N-infused Na$_2$SO$_4$ electrolyte, following electrochemical studies are performed at −1.4 V vs. SCE. Fig. 2b is the profile of NO_3^--N, NH_4^+-N, and NO_2^--N concentrations with respect to time via the potentiostatic tests (Fig. S13), where

the quantification of ion concentrations is calculated on the respective calibration curves of ultraviolet-visible absorption spectra (Figs. S14–S16). The concentration of NO_3^--N gradually decreases while the amount of NH$_3$ gradually increases, and NO_2^--N has always remained extremely low level during the electrolysis process. After only 120 min of the electrolysis, this reduction ends with an excellent NO_3^--N conversion efficiency of 93.1 ± 1.1% and high NH$_3$ selectivity of 90.9 ± 0.5% (Fig. S17). As shown in Fig. 2c, we find that the more negative the potential is, the more NO_3^- is removed, and simultaneously ammonia selectivity remains unchanged beyond − 1.4 V vs. SCE. It is noteworthy that even if the driving potential is greater than that of R_n (−1.5, −1.6, and −1.7 V vs. SCE), efficient electrochemical reduction of NO_3^--into-NH$_3$ can still take place, which has also been discovered in previous reports [36,37]. Fig. S18 shows the FE of NH$_3$ on Cu/Fe-TiO$_2$ at different potentials. We can see that as the potential becomes more and more negative, the FE of NH$_3$ shows a trend of first increase and then decrease, where the FE of NH$_3$ reaches a maximum of 91.2% at − 1.4 V vs. SCE. The reason for its decrease is the competitive hydrogen evolution reaction.

To notarize the reliability of Nessler's reagent colorimetric method,
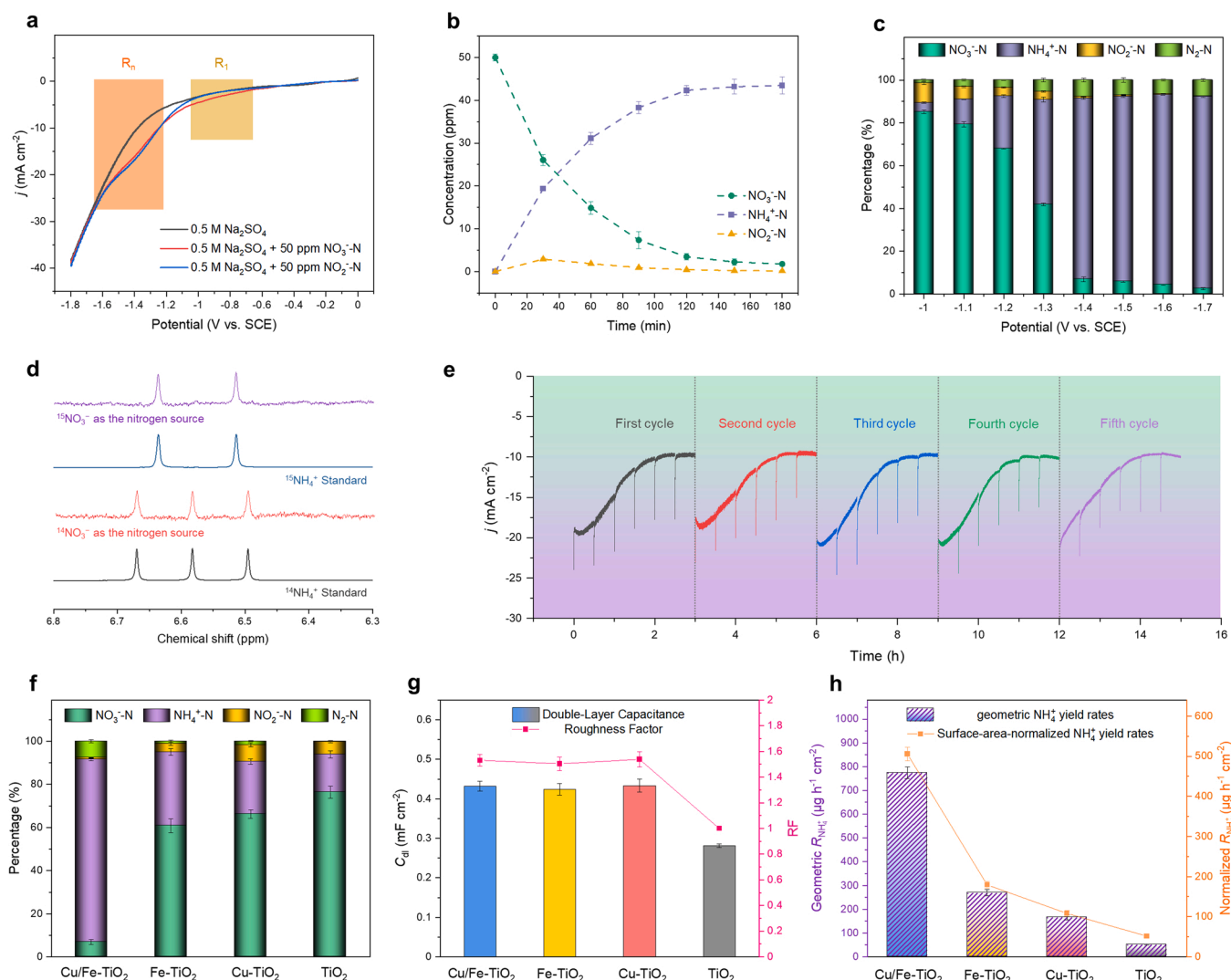
Fig. 2. Nitrate removal performance of Cu/Fe-TiO$_2$ and its counterparts. (a) Linear sweep voltammetry curves of Cu/Fe-TiO$_2$ in different electrolytes. (b) Time-dependent concentrations of NO_3^--N, NH_4^+-N, and NO_2^--N over Cu/Fe-TiO$_2$. (c) Conversion of NO_3^--N and selectivity of NH_4^+-N, NO_2^--N, and possible N$_2$-N at different potentials. (d) Comparison of ^{1}H NMR spectra of $^{14}NO_3^-$-N and $^{15}NO_3^-$-N feedstock. (e) Cycling stability of Cu/Fe-TiO$_2$ under consecutive recycling electrolysis at − 1.4 V vs. SCE, without any processing of the cathode after each recycling test. (f) Conversion efficiency and selectivity for Cu/Fe-TiO$_2$, Cu-TiO$_2$, Fe-TiO$_2$, and TiO$_2$ substrate at − 1.4 V vs. SCE. (g) Electrochemical double-layer capacitance (C_{dl}) and roughness factor (RF) of the different electrocatalysts, and (h) their geometric NH_4^+-N yield rates and surface area-normalized NH_4^+-N yield rates (intrinsic activity).

flow injection analyzer (FIA) was carried out. Next, NH_3 yield after 120 min of the electrolysis over Cu/Fe-TiO$_2$ is compared by the Nessler's reagent colorimetric method and the FIA. As shown in Fig. S19, we can see that the results of the two methods for the quantification of NH_3 are very close, indicating that the Nessler's reagent colorimetric method is reasonable to determine the content of NH_3 in this work. To further verify the safety of test environment and confirm the N origin of the generated NH_3, $^{15}NO_3^-$-N isotope labeling experiment combined with the ^1H nuclear magnetic resonance (^1H NMR) technology is undoubtedly the best-guaranteed method [38,39]. Relative to that of the $^{14}NO_3^-$-N feedstock, the ^1H NMR spectrum of $^{15}NO_3^-$-N after electrolysis presents two resonance peaks, which are consistent with the characteristic doublet coupling of standard $^{15}NH_4^+$, and meanwhile, no triplet coupling for the standard $^{14}NH_4^+$ is detected (Fig. 2d). This result forcefully bears out the fact that the formation of NH_3 derives from the NO_3^- electroreduction.

To evaluate the stability of Cu/Fe-TiO$_2$, the consecutive cycling tests were firstly performed. There are no obvious changes in the time-course current densities, the conversion efficiency of NO_3^--N, and the selectivity of generated NH_3 (Fig. 2e and S20). It should be noted that the reason for the decreased current density of each cycle is that the concentration of the reactant nitrate gradually decreases as the catalytic reaction goes on [7,12,40]. To verify whether there is the phenomenon of catalyst dissolution, we measured the concentrations of Cu^{2+} and Fe^{2+} leaching in the solution after each recycling electrolysis. The result of Table S1 shows that the leaching concentrations of Cu^{2+} and Fe^{2+} in the electrolyte after each cycle are extremely low, which is close to the lower detection limit (ppb level) of the inductively coupled plasma-atomic emission spectrometry (ICP). Besides the consecutive cycling tests, we also conducted a long-term electrocatalytic test of 10 h (Fig. S21), and performed the electrochemical NO_3^- reduction in the new electrolyte over Cu/Fe-TiO$_2$ after the long-term electrocatalytic test. As shown in Fig. S22, we can see that compared with that before the long-term electrocatalytic test, there is no obvious changes in the conversion efficiency of NO_3^--N and selectivity of generated NH_3. For another, the XRD pattern and FE-SEM image collected after electrocatalysis confirm the morphological stability of Cu/Fe-TiO$_2$ (Fig. S23). These results jointly confirm that Cu/Fe-TiO$_2$ possesses an outstanding stability for electrochemical NO_3^-RR.

To fully understand the rationale behind the high-efficiency removal activity and selectivity of Cu/Fe-TiO$_2$, we tested the performances of its counterparts of Cu-TiO$_2$, Fe-TiO$_2$, and TiO$_2$ substrate under same conditions. As shown in Fig. 2f and S24, the removal efficiency of NO_3^- and the selectivity of generated NH_3 for Cu/Fe-TiO$_2$ are 93.1 $\pm$ 1.1% and 90.9 $\pm$ 0.5%, which is clearly superior to 39.2 $\pm$ 3.2% and 86.9 $\pm$ 1.5% of Fe-TiO$_2$, 33.8 $\pm$ 1.9% and 72.1 $\pm$ 1.2% of Cu-TiO$_2$, and 23.6 $\pm$ 1.9% and 74.1 $\pm$ 1.7% of TiO$_2$ substrate, respectively, which is also supported by the results of their LSV polarization tests and electrochemical impedance spectroscopy (EIS) analysis (Figs. S25 and S26). Moreover, Cu/Fe-TiO$_2$ has an excellent FE of NH_3 with 91.2%, which is obviously higher that of Fe-TiO$_2$ (41.2%), Cu-TiO$_2$ (30.3%), and TiO$_2$ substrate (12.1%) (Fig. S27). The NO_3^-RR performance of Cu/Fe-TiO$_2$, especially in the selectivity of generated NH_3, is better than most of Cu- or Fe-based materials reported in recent studies (Table S2). On the other hand, the energy consumption (EC) and electrical energy per order (E_{EO}) is calculated to be 0.54 kWh mol^{-1} and 0.73 kWh m^{-3} for Cu/Fe-TiO$_2$, respectively, which is obviously lower than that of 1.19 kWh mol^{-1} and 2.01 kWh m^{-3} for Fe-TiO$_2$, that of 1.30 kWh mol^{-1} and 2.26 kWh m^{-3} for Cu-TiO$_2$, that of 1.45 kWh mol^{-1} and 2.58 kWh m^{-3} for TiO$_2$ substrate (Table S3). The EC and E_{EO} of Cu/Fe-TiO$_2$ is superior to the FeNi/ g-mesoC/NF and the Pd based TiO$_2$ of recent reported catalysts [8,41].

Considering with the design idea and physical characterization results, we conclude that the superior NO_3^-RR performance of Cu/Fe-TiO$_2$ is probably derived from the Cu/Fe hetero-phase interface. To exclude the performance deviation caused by the difference in the number of active sites of the catalysts, their electrochemical active surface areas

(ECSAs) were calculated by the corresponding electrochemical double-layer capacitance (C_{dl}) (Fig. 2g and S28–S31), and meanwhile, we introduced the concept of roughness factors (RFs) to evaluate their intrinsic activities (normalized NH_4^+-N yield rates) (Fig. 2h) [42,43]. Assuming that RF value of TiO$_2$ substrate is 1, we can calculate the RF value of Cu/Fe-TiO$_2$, Fe-TiO$_2$, and Cu-TiO$_2$ as 1.53, 1.50, and 1.54, respectively. The normalized NH_4^+-N yield rate of Cu/Fe-TiO$_2$ is as high as 505.73 μg h^{-1} cm^{-2}, which is approximately 4.68 and 2.82 times more than those of Cu-TiO$_2$ and Fe-TiO$_2$. This result indicates the presence of highly intrinsic active site in the Cu/Fe-TiO$_2$.

3.3. Revealing the mechanism for efficient NO_3^--into-NH_3

To determine the highly intrinsic active site in the Cu/Fe-TiO$_2$, DFT simulations were performed attentively. Based on the above physical characterization results, we construct a hetero-phase interface with (111) plane of Cu and (110) plane of Fe anchored in (110) plane of TiO$_2$ substrate as the model system (Fig. S32). For comparison, corresponding models for its counterparts of Cu-TiO$_2$ and Fe-TiO$_2$ are also built (Figs. S33 and S34). Fig. 3a displays their Gibbs free energy diagrams of *NO_3^--into-*NH_3 followed by a typical protonation pathway, involving the deoxidation reactions of *NO_3 → *NO_2 → *NO → *N and the hydrogenation reactions of *N → *NH → *NH_2 → *NH_3 (Figs. S35–S37). For Cu-TiO$_2$, the hydrogenation of *N serves as the potential determining step (PDS) with a high barrier of 1.38 eV. In contrast, the changing value of the Gibbs free energy on Cu/Fe-TiO$_2$ for *N → *NH is − 0.80 eV, making the NO_3^-RR proceed in a spontaneous direction. The presence of Fe pushes a transition of PDS from *N → *NH to *NH_2 → *NH_3 and endows Cu/Fe-TiO$_2$ with a lower barrier of 0.21 eV compared with that of Fe-TiO$_2$ (PDS, 0.56 eV). This result further confirms that Cu/ Fe hetero-phase interface is the origin of the intrinsic high activity of Cu/ Fe-TiO$_2$ for the NO_3^-RR.

As we all know, heterogeneous catalytic reactions mainly involve three processes, such as adsorption, reaction, and desorption. However, apart from the reaction itself, the adsorption and desorption are generally neglected during the entire electrochemical reaction process in previous reports. In this context, we next explore the adsorption and desorption behaviors of NO_3^- and *NH_3 on the catalytic model surfaces, respectively. The analysis of density of states (DOS) shows that the d band center of Fe is closer to the Fermi level than that of Cu (Figs. S38–S40), which leads to the antibonding states between Fe and adsorbed species being less occupied, and thus strengthening the adsorption of *NO_3 and *NH_3. Once the adsorption of NO_3^- or NH_3 on the surface of catalyst, the electron transfers occur from partially occupied d band to d-p π antibonding orbital of Fe – O or Fe – N bonds. On the other hand, the π antibonding orbitals, below the Fermi level, of Cu 3d – O 2p or Cu 3d – N 2p are fully occupied, indicating that the adsorption of NO_3^- is weak and the desorption of NH_3 is easy (Fig. 3b and S41). Specifically, the NO_3^- adsorption energy of Fe-TiO$_2$ is − 1.34 eV, which is the largest relative to that of Cu-TiO$_2$ (−0.52 eV) and Cu/Fe-TiO$_2$ (−0.44 eV), while compared with that of Fe-TiO$_2$ (0.60 eV) and/or Cu/ Fe-TiO$_2$ (1.11 eV), the *NH_3 desorption energy on Cu-TiO$_2$ of 0.35 eV is the smallest, implying that the optimal site of NO_3^- adsorption and *NH_3 desorption is the surface of Fe-TiO$_2$ and Cu-TiO$_2$, respectively (Fig. 3c).

To obtain further insight, the charge density differences and crystal orbital Hamilton populations (COHPs) of the three model systems were investigated. The interactions between *NO_3 and three models for their charge densities are shown in Fig. 4a-c. We find that there is a strong electron accumulation (blue) around O atoms of *NO_3 and an electron depletion (red) around Fe or Cu sites, where a larger electron cloud between *NO_3 and the surface of Fe-TiO$_2$ is observed compared with that of *NO_3 on the surface of Cu-TiO$_2$ and Cu/Fe-TiO$_2$, indicating that the electrons easily transfer from the partially occupied d orbitals of Fe sites to the empty p orbitals of NO_3^- molecules. The results agree well with the obtained adsorption energy of NO_3^- on catalytic model surface. In addition, the dispersed O $2p$ orbitals of NO_3^- after surface adsorption
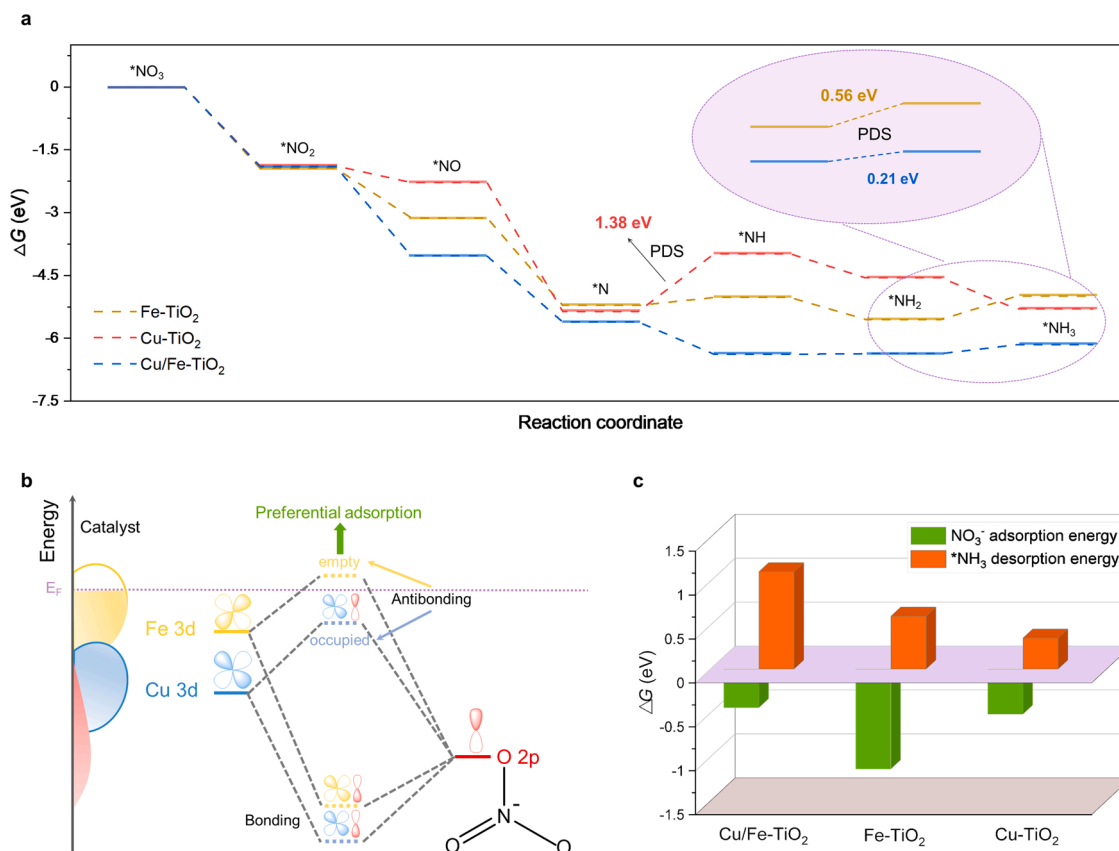
Fig. 3. DFT calculation of NO_3^--into-NH_3 on the surface of catalysts. (a) Calculated free energy diagram of Cu/Fe-TiO_2, Cu-TiO_2, and Fe-TiO_2 at the equilibrium potential. (b) Schematic of the formation of metal $-$ O bonds, E_F represents the Fermi level. (c) Free energy of the NO_3^- adsorption and *NH_3 desorption on Cu/Fe-TiO_2, Cu-TiO_2, and Fe-TiO_2.

indicates that the hybridization of *d-p* orbitals is responsible for inter-atomic interaction (Figs. S42–S47). To quantify the bond strength of Fe – O / Cu – O, Fig. 4d-f displays the corresponding COHPs, where the bonding, occupied anti-bonding, and empty orbitals are on the right (light purple area), left (light grey area), and upward (white area) sides, respectively. Benefitting from the upper occupied *d* orbitals of Fe, the Fe – O bond shows more significant anti-bonding orbital above Fermi level than that of Cu – O bond. Strikingly, the value of integrated COHP (ICOHP) up to the Fermi level for the Fe – O bond on Cu/Fe hetero-phase interface is − 2.02 eV, which is more negative than that of the Fe_1 – O_1 bond (−1.73 eV) and Fe_2 – O_2 (−1.66 eV) bond in Fe-TiO_2, indicating that the Fe – O bond is more stable on Cu/Fe hetero-phase interface. Combining the Lowest Energy Principle with the above-mentioned adsorption energy analysis, the NO_3^- preferentially adsorbs to the in-plane Fe phase in Cu/Fe-TiO_2, and then intelligently switches towards the Cu/Fe hetero-phase interface by the stronger force of Fe – O bond in Cu/Fe interface [44,45]. Correspondingly, the results of charge density differences, density of states, COHPs, and ICOHPs also suggest that compared with the model systems of Fe-TiO_2 and Cu/Fe-TiO_2, the desorption of *NH_3 occurs most easily from the surface of Cu-TiO_2 (Fig. 4g-i and S48–S51). As a consequence, the stronger Fe – O bond and weaker Cu – N bond indicate that the NO_3^- adsorption and *NH_3 desorption are favored on the Fe and Cu sites, respectively.

Next, we employ in situ ATR-SEIRAS technology to shed light on the reaction mechanism by identifying the key intermediates adsorbed on the model surfaces. From Fig. 5a, it can be found that with the negative shift of the applied potential, there is an obvious peak appeared at 1494 cm^{-1}, which is attributed to the N – H stretching/bending mode in NH_3 [46,47]. This result further confirms the occurrence of electrochemical reduction from NO_3^- to NH_3, which is also corroborated from the broadening peak at about 3460 cm^{-1} [48,49]. Moreover,

ATR-SEIRAS measurements for the three samples at the same test conditions were also investigated thoroughly (Fig. 5b). A typical signal at 1110 cm^{-1} is indexed to *SO_4 species from the electrolyte on electrode surface, while the peaks of *NO_3 and *NO_2 are observed at 948 and 1241 cm^{-1}, respectively [48,50–52]. It is worth noting that the peak intensity of *NH_3 at 1494 cm^{-1} for Fe-TiO_2 is the strongest, indicating that the more *NH_3 accumulates on the surface of Fe, the stronger the interaction between *NH_3 and Fe-TiO_2 is. In contrast, the interaction between *NH_3 and Cu-TiO_2 is weaker than that between *NH_3 and Fe-TiO_2, thereby rendering the in-plane Cu phase of Cu/Fe-TiO_2 more conducive for the desorption of *NH_3 during the NO_3^-RR as proven by the above COHP calculations.

Considering the results of the experimental in situ ATR-SEIRAS and theoretical calculations, a potentially SASS pathway for the whole NO_3^-RR process over the Cu/Fe-TiO_2 catalyst can be proposed based on the thermodynamic nature of bonding (Fig. 5c). Initially, the NO_3^- in the electrolyte is adsorbed on the in-plane Fe phase of Cu/Fe-TiO_2. The adsorbed *NO_3 species intelligently switches towards the Cu/Fe hetero-phase interface and then are reduced to *NH_3 through a continuous protonation hydrogenation process. Finally, the adsorbed *NH_3 switches further towards the in-plane Cu phase of Cu/Fe-TiO_2 to favor the desorption of *NH_3 from the cathode. Following this SASS pathway, the conversion of NO_3^--into-NH_3 can be improved by overcoming the lowest endothermic energy barrier. Therefore, the mechanism of the switching of the active sites for the adsorption/desorption of key intermediates should be given sufficient research attention, especially for multi-component complex electrocatalytic reactions, such as the carbon dioxide reduction reaction (CO_2RR), oxygen reduction reaction (ORR), and urea electrosynthesis by integrating CO_2RR with NO_3^-RR.
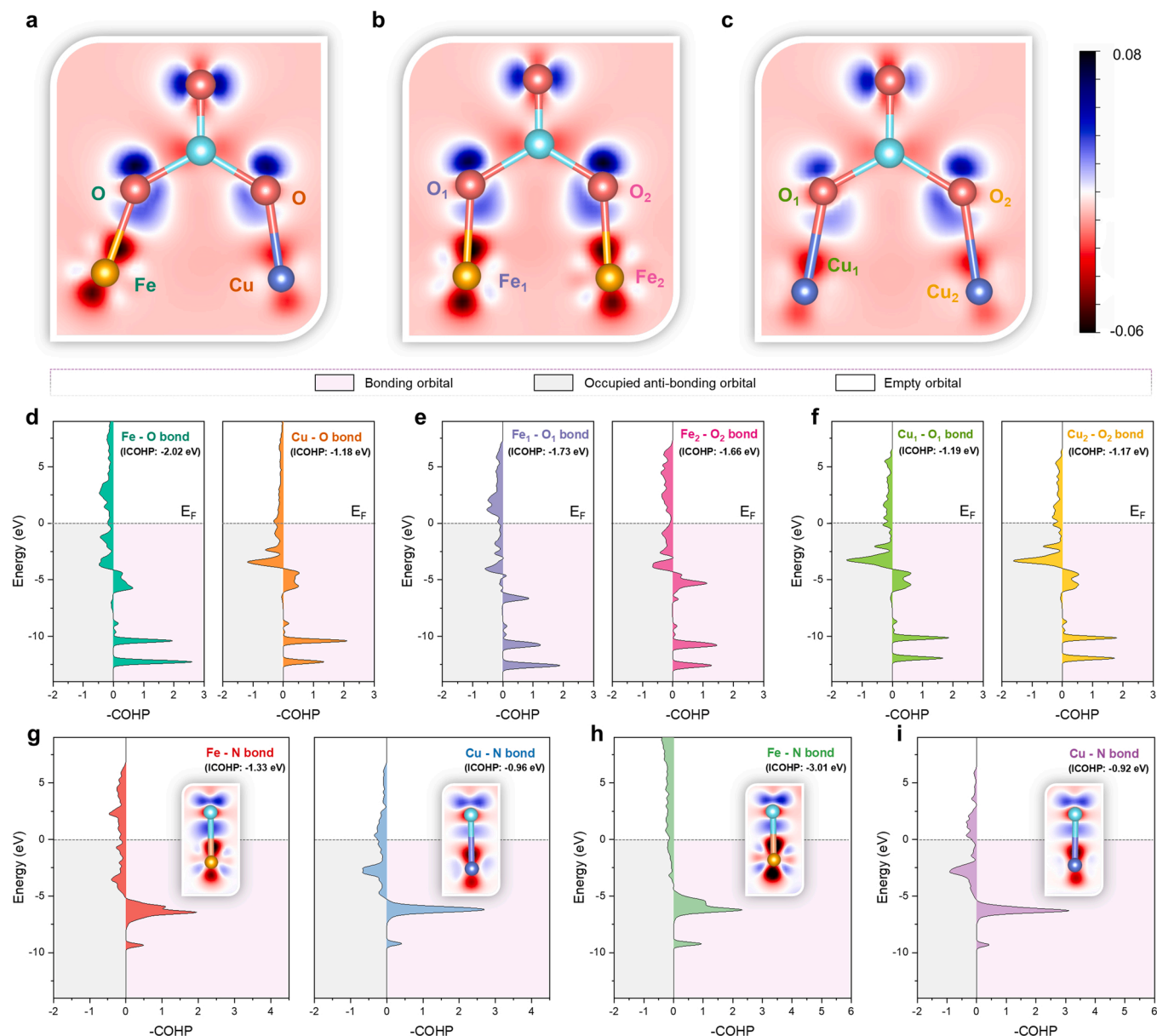
Fig. 4. Analysis of electrons and chemical bonds over the catalytic reactive sites. (a), (b), (c) Electron density of the *NO_3 on the surface of Cu/Fe-TiO_2, Fe-TiO_2, and Cu-TiO_2, respectively. (d), (e), (f) Crystal orbital Hamilton populations (COHP) of the Fe – O and Cu – O bonds in Cu/Fe-TiO_2, the Fe_1 – O_1 and Fe_2 – O_2 bonds in Fe-TiO_2, and the Cu_1 – O_1 and Cu_2 – O_2 bonds in Cu-TiO_2 with adsorbed *NO_3, respectively. The corresponding integrated COHPs (ICOHP) are also calculated in inset d, e, f. (g), (h), (i) COHP of the Fe – N bond and Cu – N bond in Cu/Fe-TiO_2, the Fe – N bond in Fe-TiO_2, and the Cu – N bond in Cu-TiO_2 with adsorbed *NH_3, respectively. Insets in g, h, i show the corresponding electron densities and ICOHPs.

4. Conclusions

In summary, we have demonstrated, for the first time, the sequential active-site-switching (SASS) mechanism on the model catalytic system of Cu/Fe-TiO_2 for the efficient electrochemical conversion of NO_3^--into-NH_3. Following this mechanism, the optimal active sites for the adsorption of NO_3^-, reduction of *NO_3 into *NH_3, and desorption of *NH_3 are the in-plane Fe phase, Cu/Fe hetero-phase interface, and in-plane Cu phase in the Cu/Fe-TiO_2, respectively. The two active-site switches for the *NO_3 and *NH_3 can reduce the energy barrier for the entire reaction considerably, expediting the conversion of NO_3^--into-NH_3. Benefitting from the SASS pathway, Cu/Fe-TiO_2 exhibits superior NO_3^-RR performance with NO_3^- removal efficiency, NH_3 selectivity, and FE of $93.1 \pm 1.1\%$, $90.9 \pm 0.5\%$, and 91.2%, respectively. These performance parameters are superior to those of most recently reported Cu- or Fe-based electrocatalysts. Moreover, Cu/Fe-TiO_2 does not exhibit considerable loss of activity and selectivity even after consecutive cycling and long-term electrocatalytic tests. On the other hand, the EC and E_{EO} of Cu/Fe-TiO_2 is only 0.54 kWh mol^{-1} and 0.73 kWh m^{-3}, which is superior to the FeNi/g-mesoC/NF and the Pd based TiO_2 of recent reported catalysts. $^{15}NO_3^-$-N isotope labeling and ^{1}H NMR experiments confirm the origin of N in the generated NH_3, which ascertain the safety of test environment. Moreover, the intrinsic activity of Cu/Fe-TiO_2 normalized by the RF is approximately 4.68- and 2.82-fold larger than that of Cu-TiO_2 and Fe-TiO_2, respectively. This finding not only offers a novel perspective for exploring the NO_3^-RR mechanism and developing highly efficient catalysts but also opens up a window for the studies of other electrochemical redox reactions.

CRediT authorship contribution statement

X.H.Y. H.L. and F.J.Y. developed the research concept. X.H.Y., S.W.,
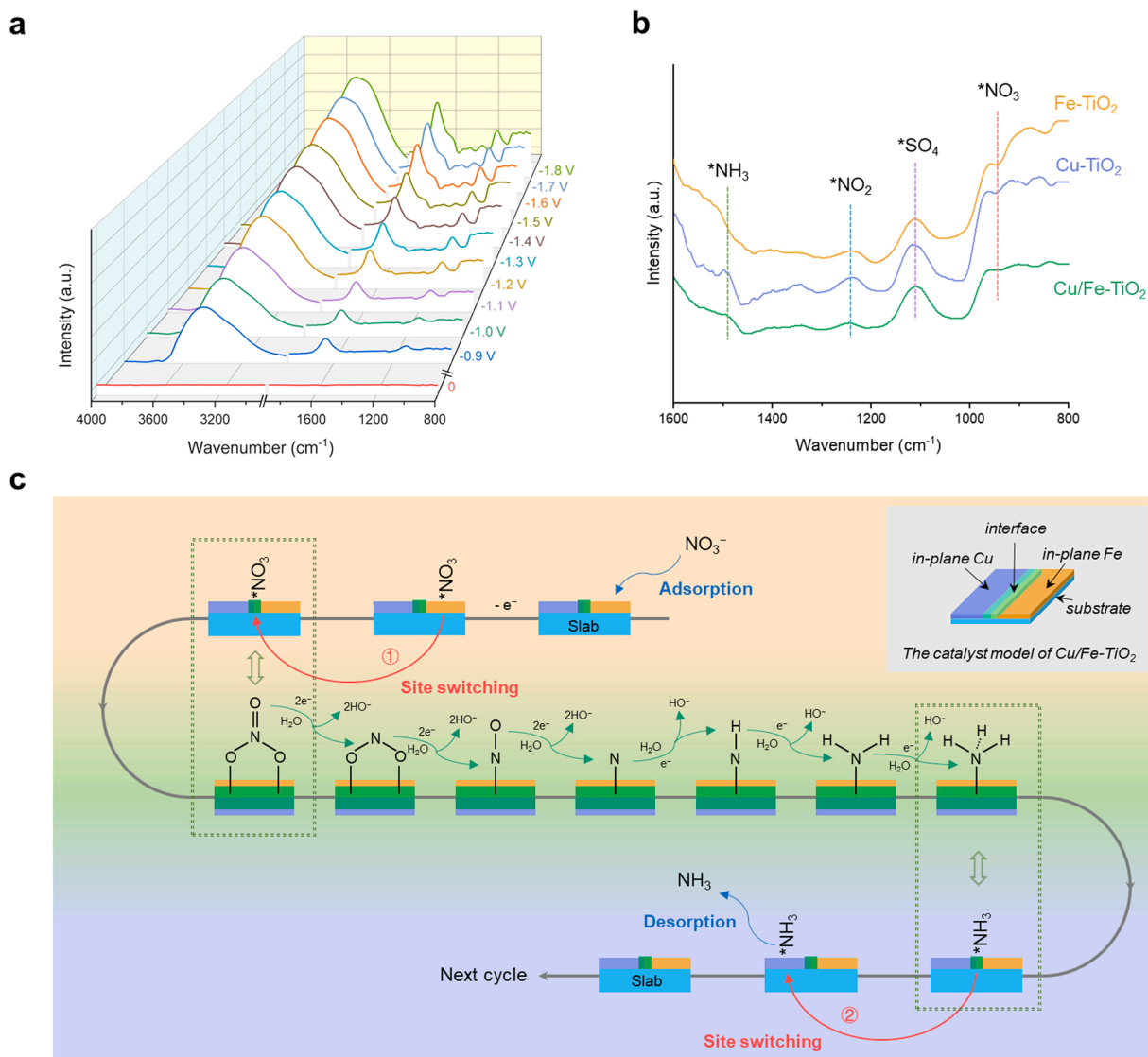
Fig. 5. *In situ* infrared spectra of the catalysts and schematic of the sequential active-site-switching mechanism over Cu/Fe-TiO₂ catalyst. (a) *In situ* attenuated total reflection Fourier transform infrared spectroscopy (ATR-SEIRAS) of the electrocatalytic reduction of NO₃⁻ over Cu/Fe-TiO₂ different applied potentials. (b) ATR-SEIRAS spectra of Cu/Fe-TiO₂, Fe-TiO₂, and Cu-TiO₂ at − 1.4 V vs. SCE. (c) Optimal reaction pathway, defined as the sequential active-site-switching mechanism, for NO₃⁻RR over Cu/Fe-TiO₂ with the Cu/Fe hetero-phase interface.

and C.S. prepared the materials, performed the electrochemical experiments, and analyzed the data. R.W. and X.H.Y. provided the theoretical calculations. X.H.Y., H.L., and R.W. contributed to the interpretation of the results and the writing of the manuscript, which was revised by S.L. and L.F. All authors contributed to the scientific discussions.

Declaration of Competing Interest

The authors declare no conflict of interest.

Data Availability

Data will be made available on request.

Acknowledgements

Appendix A. Supporting information

Supplementary data associated with this article can be found in the online version at doi:10.1016/j.apcatb.2023.122360.

References

[1] Y. Wang, C. Wang, M. Li, Y. Yu, B. Zhang, Nitrate electroreduction: mechanism insight, in situ characterization, performance evaluation, and challenges, Chem. Soc. Rev. 50 (2021) 6720–6733.

[2] A.S. Fajardo, P. Westerhoff, C.M. Sanchez-Sanchez, S. Garcia-Segura, Earth-abundant elements a sustainable solution for electrocatalytic reduction of nitrate, Appl. Catal. B: Environ. 281 (2021), 119465.

[3] H. Xu, Y. Ma, J. Chen, W.X. Zhang, J. Yang, Electrocatalytic reduction of nitrate - a step towards a sustainable nitrogen cycle, Chem. Soc. Rev. 51 (2022) 2710–2758.

[4] Q. Gao, H.S. Pillai, Y. Huang, S. Liu, Q. Mu, X. Han, Z. Yan, H. Zhou, Q. He, H. Xin, H. Zhu, Breaking adsorption-energy scaling limitations of electrocatalytic nitrate reduction on intermetallic CuPd nanocubes by machine-learned insights, Nat. Commun. 13 (2022) 2338.

[5] X. Zhang, Y. Wang, C. Liu, Y. Yu, S. Lu, B. Zhang, Recent advances in non-noble metal electrocatalysts for nitrate reduction, Chem. Eng. J. 403 (2021) 126269.

[6] Y. Wang, A. Xu, Z. Wang, L. Huang, J. Li, F. Li, J. Wicks, M. Luo, D.H. Nam, C. S. Tan, Y. Ding, J. Wu, Y. Lum, C.T. Dinh, D. Sinton, G. Zheng, E.H. Sargent, Enhanced nitrate-to-ammonia activity on copper-nickel alloys via tuning of intermediate adsorption, J. Am. Chem. Soc. 142 (2020) 5702–5708.

[7] Y. Wang, W. Zhou, R. Jia, Y. Yu, B. Zhang, Unveiling the activity origin of a copper-based electrocatalyst for selective nitrate reduction to ammonia, Angew. Chem. Int. Ed. 59 (2020) 5350–5354.

[8] X. Chen, T. Zhang, M. Kan, D. Song, J. Jia, Y. Zhao, X. Qian, Binderless and oxygen vacancies rich FeNi/graphitized mesoporous carbon/Ni foam for electrocatalytic reduction of nitrate, Environ. Sci. Technol. 54 (2020) 13344–13353.

[9] L. Su, K. Li, H. Zhang, M. Fan, D. Ying, T. Sun, Y. Wang, J. Jia, Electrochemical nitrate reduction by using a novel Co_3O_4/Ti cathode, Water Res. 120 (2017) 1–11.

[10] X. Yang, J. Wan, H. Zhang, Y. Wang, In situ modification of the d-band in the core–shell structure for efficient hydrogen storage via electrocatalytic N_2 fixation, Chem. Sci. 13 (2022) 11030–11037.

[11] J.M. McEnaney, S.J. Blair, A.C. Nielander, J.A. Schwalbe, D.M. Koshy, M. Cargnello, T.F. Jaramillo, Electrolyte engineering for efficient electrochemical nitrate reduction to ammonia on a titanium electrode, ACS Sustain. Chem. Eng. 8 (2020) 2672–2681.

[12] S. Zhang, M. Li, J. Li, Q. Song, X. Liu, High-ammonia selective metal-organic framework-derived Co-doped Fe/Fe_2O_3 catalysts for electrochemical nitrate reduction, Proc. Natl. Acad. Sci. 119 (2022) e2115504119.

[13] W.J. Sun, H.Q. Ji, L.X. Li, H.Y. Zhang, Z.K. Wang, J.H. He, J.M. Lu, Built-in electric field triggered interfacial accumulation effect for efficient nitrate removal at ultra-low concentration and electroreduction to ammonia, Angew. Chem. Int. Ed. 60 (2021) 22933–22939.

[14] Z. Fang, Z. Jin, S. Tang, P. Li, P. Wu, G. Yu, Porous two-dimensional iron-cyano nanosheets for high-rate electrochemical nitrate reduction, ACS Nano 16 (2021) 1072–1081.

[15] Y. Wang, H. Li, W. Zhou, X. Zhang, B. Zhang, Y. Yu, Structurally disordered RuO_2 nanosheets with rich oxygen vacancies for enhanced nitrate electroreduction to ammonia, Angew. Chem. Int. Ed. 134 (2022) e202202604.

[16] N. Singh, B.R. Goldsmith, Role of electrocatalysis in the remediation of water pollutants, ACS Catal. 10 (2020) 3365–3371.

[17] P.H. Van Langevelde, I. Katsounaros, M.T.M. Koper, Electrocatalytic nitrate reduction for sustainable ammonia production, Joule 5 (2021) 290–294.

[18] H. Liu, X. Lang, C. Zhu, J. Timoshenko, M. Ruscher, L. Bai, N. Guijarro, H. Yin, Y. Peng, J. Li, Z. Liu, W. Wang, B.R. Cuenya, J. Luo, Efficient electrochemical nitrate reduction to ammonia with copper-supported rhodium cluster and single-atom catalysts, Angew. Chem. Int. Ed. (2022), e202202556.

[19] Z.Y. Wu, M. Karamad, X. Yong, Q. Huang, D.A. Cullen, P. Zhu, C. Xia, Q. Xiao, M. Shakouri, F. Chen, J.Y.T. Kim, Y. Xia, K. Heck, Y. Hu, M.S. Wong, Q. Li, I. Gates, S. Siahrostami, H. Wang, Electrochemical ammonia synthesis via nitrate reduction on Fe single atom catalyst, Nat. Commun. 12 (2021) 2870.

[20] S. Garcia-Segura, M. Lanzarini-Lopes, K. Hristovski, P. Westerhoff, Electrocatalytic reduction of nitrate: Fundamentals to full-scale water treatment applications, Appl. Catal. B: Environ. 236 (2018) 546–568.

[21] W. He, J. Zhang, S. Dieckhofer, S. Varhade, A.C. Brix, A. Lielpetere, S. Seisel, J.R. C. Junqueira, W. Schuhmann, Splicing the active phases of copper/cobalt-based catalysts achieves high-rate tandem electroreduction of nitrate to ammonia, Nat. Commun. 13 (2022) 1129.

[22] T. Zhu, Q. Chen, P. Liao, W. Duan, S. Liang, Z. Yan, C. Feng, Single-atom Cu catalysts for enhanced electrocatalytic nitrate reduction with significant alleviation of nitrite production, Small 16 (2020) e2004526.

[23] G.A. Cerrón-Calle, A.S. Fajardo, C.M. Sánchez-Sánchez, S. Garcia-Segura, Highly reactive Cu-Pt bimetallic 3D-electrocatalyst for selective nitrate reduction to ammonia, Appl. Catal. B: Environ. 302 (2022), 120844.

[24] Y. Xu, K. Ren, T. Ren, M. Wang, M. Liu, Z. Wang, X. Li, L. Wang, H. Wang, Cooperativity of Cu and Pd active sites in CuPd aerogels enhances nitrate electroreduction to ammonia, Chem. Commun. 57 (2021) 7525–7528.

[25] C. Wang, Z. Liu, T. Hu, J. Li, L. Dong, F. Du, C. Li, C. Guo, Metasequoia-like nanocrystal of iron-doped copper for efficient electrocatalytic nitrate reduction into ammonia in neutral media, ChemSusChem 14 (2021) 1825–1829.

[26] F.Y. Chen, Z.Y. Wu, S. Gupta, D.J. Rivera, S.V. Lambeets, S. Pecaut, J.Y.T. Kim, P. Zhu, Y.Z. Finfrock, D.M. Meira, G. King, G. Gao, W. Xu, D.A. Cullen, H. Zhou, Y. Han, D.E. Perea, C.L. Muhich, H. Wang, Efficient conversion of low-concentration nitrate sources into ammonia on a Ru-dispersed Cu nanowire electrocatalyst, Nat. Nanotechnol. 17 (2022) 759–767.

[27] J. Zhu, L. Hu, P. Zhao, L.Y.S. Lee, K.-Y. Wong, Recent advances in electrocatalytic hydrogen evolution using nanoparticles, Chem. Rev. 120 (2019) 851–918.

[28] Y. Shi, B. Zhang, Recent advances in transition metal phosphide nanomaterials: synthesis and applications in hydrogen evolution reaction, Chem. Soc. Rev. 45 (2016) 1529–1541.

[29] R.D. Milton, S.D. Minteer, Enzymatic bioelectrosynthetic ammonia production: recent electrochemistry of nitrogenase, nitrate reductase, and nitrite reductase, ChemPlusChem 82 (2017) 513–521.

[30] C.L. Ford, Y.J. Park, E.M. Matson, Z. Gordon, A.R. Fout, A bioinspired iron catalyst for nitrate and perchlorate reduction, Science 354 (2016) 741–743.

[31] Y. Li, J. Zhang, Q. Chen, X. Xia, M. Chen, Emerging of heterostructure materials in energy storage: A review, Adv. Mater. 33 (2021), e2100855.

[32] J. Klimeš, D.R. Bowler, A. Michaelides, Van der Waals density functionals applied to solids, Phys. Rev. B 83 (2011), 195131.

[33] G. Kresse, D. Joubert, From ultrasoft pseudopotentials to the projector augmented-wave method, Phys. Rev. B 59 (1999) 1758.

[34] G. Kresse, J. Furthmüller, Efficiency of ab-initio total energy calculations for metals and semiconductors using a plane-wave basis set, Comput. Mater. Sci. 6 (1996) 15–50.

[35] G. Kresse, J. Furthmüller, Efficient iterative schemes for ab initio total-energy calculations using a plane-wave basis set, Phys. Rev. B 54 (1996) 11169.

[36] F. Yao, M. Jia, Q. Yang, F. Chen, Y. Zhong, S. Chen, L. He, Z. Pi, K. Hou, D. Wang, X. Li, Highly selective electrochemical nitrate reduction using copper phosphide self-supported copper foam electrode: Performance, mechanism, and application, Water Res. 193 (2021), 116881.

[37] R. Mao, N. Li, H. Lan, X. Zhao, H. Liu, J. Qu, M. Sun, Dechlorination of trichloroacetic acid using a noble metal-free graphene-Cu foam electrode via direct cathodic reduction and atomic H, Environ. Sci. Technol. 50 (2016) 3829–3837.

[38] X. Yang, F. Ling, J. Su, X. Zi, H. Zhang, H. Zhang, J. Li, M. Zhou, Y. Wang, Insights into the role of cation vacancy for significantly enhanced electrochemical nitrogen reduction, Appl. Catal. B: Environ. 264 (2020), 118477.

[39] Y. Wang, M.M. Shi, D. Bao, F.L. Meng, Q. Zhang, Y.T. Zhou, K.H. Liu, Y. Zhang, J. Z. Wang, Z.W. Chen, D.P. Liu, Z. Jiang, M. Luo, L. Gu, Q.H. Zhang, X.Z. Cao, Y. Yao, M.H. Shao, Y. Zhang, X.B. Zhang, J.G. Chen, J.M. Yan, Q. Jiang, Generating defect-rich bismuth for enhancing the rate of nitrogen electroreduction to ammonia, Angew. Chem. Int. Ed. 58 (2019) 9464–9469.

[40] G.-F. Chen, Y. Yuan, H. Jiang, S.-Y. Ren, L.-X. Ding, L. Ma, T. Wu, J. Lu, H. Wang, Electrochemical reduction of nitrate to ammonia via direct eight-electron transfer using a copper–molecular solid catalyst, Nat. Energy 5 (2020) 605–613.

[41] P. Gayen, J. Spataro, S. Avasarala, A.M. Ali, J.M. Cerrato, B.P. Chaplin, Electrocatalytic reduction of nitrate using magneli phase TiO_2 reactive electrochemical membranes doped with Pd-based catalysts, Environ. Sci. Technol. 52 (2018) 9370–9379.

[42] L. Hu, A. Khaniya, J. Wang, G. Chen, W.E. Kaden, X. Feng, Ambient electrochemical ammonia synthesis with high selectivity on Fe/Fe oxide catalyst, ACS Catal. 8 (2018) 9312–9319.

[43] X. Yang, F. Ling, X. Zi, Y. Wang, H. Zhang, H. Zhang, M. Zhou, Z. Guo, Y. Wang, Low-coordinate step atoms via plasma-assisted calcinations to enhance electrochemical reduction of nitrogen to ammonia, Small 16 (2020), e2000421.

[44] V. Fung, Z. Wu, D.E. Jiang, New bonding model of radical adsorbate on lattice oxygen of perovskites, J. Phys. Chem. Lett. 9 (2018) 6321–6325.

[45] B.M. Comer, J. Li, F. Abild-Pedersen, M. Bajdich, K.T. Winther, Unraveling electronic trends in O* and OH* surface adsorption in the MO_2 transition-metal oxide series, J. Phys. Chem. C 126 (2022) 7903–7909.

[46] Y. Huang, J. Long, Y. Wang, N. Meng, Y. Yu, S. Lu, J. Xiao, B. Zhang, Engineering nitrogen vacancy in polymeric carbon nitride for nitrate electroreduction to ammonia, ACS Appl. Mater. Interfaces 13 (2021) 54967–54973.

[47] I. Katsounaros, M.C. Figueiredo, X. Chen, F. Calle-Vallejo, M.T. Koper, Structure- and coverage-sensitive mechanism of NO reduction on platinum electrodes, ACS Catal. 7 (2017) 4660–4667.

[48] F. Ovalles, M. Gallignani, R. Rondón, M.R. Brunetto, R. Luna, Determination of sulphate for measuring magnesium sulphate in pharmaceuticals by flow analysis-Fourier transforms infrared spectroscopy, Lat. Am. J. Pharm. 28 (2009) 173–182.

[49] P. Li, Z. Zhou, Q. Wang, M. Guo, S. Chen, J. Low, R. Long, W. Liu, P. Ding, Y. Wu, Y. Xiong, Visible-light-driven nitrogen fixation catalyzed by Bi_5O_7Br nanostructures: enhanced performance by oxygen vacancies, J. Am. Chem. Soc. 142 (2020) 12430–12439.

[50] S. Polat, P. Sayan, Characterization and kinetics of calcium sulfate dihydrate crystallization in the presence of trimesic acid, Asia-Pac. J. Chem. Eng. 12 (2017) 391–399.

[51] J. Li, R. Chen, J. Wang, Y. Zhou, G. Yang, F. Dong, Subnanometric alkaline-earth oxide clusters for sustainable nitrate to ammonia photosynthesis, Nat. Commun. 13 (2022) 1098.

[52] M.C. Figueiredo, J. Solla-Gullón, F.J. Vidal-Iglesias, V. Climent, J.M. Feliu, Nitrate reduction at Pt(100) single crystals and preferentially oriented nanoparticles in neutral media, Catal. Today 202 (2013) 2–11.